Structural, optical and X-ray attenuation properties of Tb^{3+}:$Ba_xCe_{1-x}F_{3-x}$ (x=0.18 – 0.48) nanospheres synthesized in polyol medium.

Daniel González-Mancebo,[a] *Ana Isabel Becerro,*[*,a] *Cécile Genevois,*[b] *Mathieu Allix,*[b] *Ariadna Corral,*[c] *Angel Parrado-Gallego,*[c] *Manuel Ocaña.*[a]

[a]Instituto de Ciencia de Materiales de Sevilla (CSIC-US), c/Américo Vespucio, 49, 41092 Seville, Spain.

[b]CNRS, CEMHTI UPR3079, Universite Orléans, F-45071 Orléans, France.

[c]Centro Nacional de Aceleradores (CNA) (Universidad de Sevilla, Junta de Andalucía, CSIC), c/ Thomas Alva Edison 7, 41092, Isla de la Cartuja, Sevilla, Spain.

* corresponding author e-mail address: anieto@icmse.csic.es Phone no: +34 954489545

Abstract

Uniform $Ba_{0.18}Ce_{0.82}F_{2.82}$ nanospheres have been obtained after aging at 120 ºC for 20 hours a solution of barium and cerium nitrates and sodium tetrafluoroborate in a mixture of ethylene glycol and water. The spheres diameter could be tailored from 65 nm to 80 nm by varying the $NaBF_4$ concentration while maintaining their colloidal stability in aqueous suspension. Increasing aging temperature led to a phase transformation from hexagonal to cubic symmetry and to a concomitant increase of the Ba/Ce ratio, which reached a value close to the nominal one (50/50) at 240ºC. The same method was successful to obtain Tb^{3+}-doped nanospheres with homogeneous cations distribution and the same morphological features as the undoped material. An intense green emission was observed after excitation of the Tb^{3+}-doped samples through the Ce^{3+}-Tb^{3+} energy transfer (ET) band. The ET efficiency increased with increasing Tb content, the maximum emission being observed for the 10% Tb-doped nanospheres. Aqueous suspensions of the later sample showed excellent X-ray attenuation values that were superior to those of an iodine-based clinically approved contrast agent. Their fluorescence and X-ray attenuation properties make this material a potential dual bioprobe for luminescence bioimaging and X-rays computed tomography.

INTRODUCTION

Lanthanide-doped rare earth nanoparticles (Ln:RE NPs) are considered as promising candidates for multimodal bioimaging, owing to the unique electronic, optical and magnetic properties of lanthanide ions.[1,2] Firstly, Ln:RE NPs can be employed as excellent luminescent bioprobes in view of their superior luminescence features, such as narrow emission band widths (<10 nm), large Stokes or anti-Stokes shift, and long luminescence lifetimes, owing to the intra-*4f* transitions of the Ln^{3+} electrons, shielded by the outer *5s* and *5p* electrons. In addition, several Ln:RE NPs have been proposed as contrast agents for X-ray computed tomography (CT) because of their large X-ray attenuation factor arising from the high atomic number of lanthanides.[3,4]. Finally, some Ln^{3+} ions (Gd^{3+}, Dy^{3+} and Ho^{3+}) show good ability to relax the water protons, which make these Ln-based NPs potent contrast agents in magnetic resonance imaging.[5,6] Combination of two or three of the mentioned modalities in a single Ln:RE NP make these materials very promising candidates as imaging bioprobes.

It is well known that particle size and shape may affect the luminescence properties of Ln:RE NPs and that their uniformity is especially important to assure homogeneous properties all through the material.[78,9] In addition, for *in vivo* biomedical applications, such as the above-mentioned bioimaging techniques, the particle size is especially relevant because it affects their cellular uptake, biodistribution, circulation half-life, and excretion pathways. The optimum size is considered to be between 10 nm and 100 nm, depending on the particular application, although the ideal value is still a matter of study and it is likely that the optimal NP design will be disease-specific.[10] Hydrophilicity is another important requisite to be fulfilled by NPs for bioapplications, as they need to be compatible with the physiological fluids.[11]

Among the Ln:RE NPs, Ln:RE fluorides present certain advantages over the oxygen-based compounds. These are related to the low phonon energy of their crystal lattices that decreases the non-radiative relaxation probability, which eventually increases the luminescence efficiency.[12,13] So far, Ln:RE fluorides including REF_3 (RE = Y, La, Ce, Gd)[14,15,16,17] and $AREF_4$ (A = Li, Na, K, and RE= Y, La, Gd, Lu)[18,19,20] have been widely synthesized in the form of uniform, nanometer size particles and their properties and applications in optoelectronics and biotechnology have been intensively studied. Compared with the fluorides mentioned above, alkaline-earth lanthanide ternary fluorides

have been paid relatively little attention, although some of them, like $BaYF_5$ and $BaLuF_5$, have proved excellent luminescence properties.[21,22] The Ba-Ce fluoride system is especially underexplored, with just a few papers published on nanoparticles with $Ba_{0.2}Ce_{0.8}F_{2.8}$ and $BaCeF_5$ stoichiometry and cubic symmetry in both cases. The former were synthesized in the presence of oleic acid as capping agent, which renders 6 nm hydrophobic NPs. Their hydrophobic nature makes these NPs not suitable for bioapplications and complex postsynthesis methods are necessary to make them water-dispersible.[23] The later ($BaCeF_5$ NPs) were synthesized in isopropyl alcohol from Ce, Ba and F precursors that did not allow controlling NPs shape and size, which eventually resulted in aggregated, non-uniform NPs with an average size of 80 nm.[24] Nevertheless, the excellent luminescence properties of the $Ba_xCe_{1-x}F_{3-x}$ fluoride NPs were demonstrated in both cases.

Herein we report the synthesis of uniform, water dispersible Tb-doped $Ba_xCe_{1-x}F_{3-x}$ nanospheres with hexagonal symmetry and explore, for the first time in literature, their luminescence and X-ray attenuation and *in vitro* imaging properties to be used as bimodal bioprobes. The spherical NPs were obtained by homogeneous precipitation, in a mixture of ethylene glycol and water, through the controlled release of fluoride ions from $NaBF_4$. The influence of experimental parameters, such as precursor´s nature and concentration, polyol nature, polyol/water ratio, aging time and aging temperature, is studied in detail revealing the critical role played by each one on the morphology, chemical composition and crystalline structure of the resulting particles. The luminescence properties of the Tb-doped Ba-Ce fluoride NPs having different Tb^{3+} doping levels are evaluated to determine the optimum Tb^{3+} concentration. Finally, the ability of the obtained NPs to attenuate X-rays is analysed and compared with that of Iohexol, a clinically approved CT contrast agent.

EXPERIMENTAL SECTION

Materials

Barium nitrate ($Ba(NO_3)_2$, ≥ 99%), cerium nitrate hexahydrate ($Ce(NO_3)_3 \cdot 6H_2O$, 99%), terbium nitrate pentahydrate ($Tb(NO_3)_3 \cdot 5H_2O$, 99.9%), sodium tetrafluoroborate ($NaBF_4$, ≥ 98%), ethylene glycol (EG, $C_2H_6O_2$, 99.5%), and Iohexol (5-[N-(2,3-

Dihydroxypropyl)acetamido]-2,4,6-triiodo-N,N′-bis(2,3-ihydroxypropyl) isophthalamide, analytical standard, ≥ 95%) were purchased from Sigma Aldrich.

Synthesis of the Ba-Ce fluoride nanoparticles

Barium-cerium fluoride NPs were obtained according to the following method: $Ba(NO_3)_2$ (0.3 mmoles) and $Ce(NO_3)_3$ (0.3 mmoles) were dissolved in 3.0 mL of a mixture of EG and water (90/10 V/V) while variable amounts of sodium tetrafluoroborate were dissolved in another 3.0 mL of the same solvent mixture. Each solution was magnetically stirred at room temperature for 2 hours. The $NaBF_4$ solution was then added to the cations one and the resulting solution was magnetically stirred for 5 minutes to favour homogenization. The final solution was aged for 20 hours in tightly closed test tubes using an oven preheated at 120 ºC. The resulting dispersion was cooled down to room temperature, centrifuged to remove the supernatants and washed twice with ethanol and once with double distilled water. For some analyses, the powders were dried at room temperature. Some experiments were carried out at different temperature and time to analyse the influence of these parameters on the NPs morphology, crystal structure and chemical composition. The Tb^{3+}-doped NPs were synthesized following the same procedure and adding terbium nitrate in variable amounts from 2.5% to 15% (Tb/Ce molar %), while keeping the same concentration of $Ba(NO_3)_3$ (0.05 M) and $Ce(NO_3)_3$ (0.05 M).

Characterization techniques

The shape and size of the NPs was examined by scanning electron microscopy (SEM-FEG, Hitachi S4800). Particles size distributions were obtained from the micrographs by counting several hundreds of particles, using the free software *ImageJ*. Additional information on the size and colloidal stability of the particles in aqueous suspensions (0.5 mg mL^{-1} of solid) was obtained from Dynamic Light Scattering (DLS) measurements. These experiments were carried out using a Malvern Zetasizer Nano-ZS90 equipment, which also was used to measure the Zeta potential of the suspensions.

Ba, Ce and Tb distribution in individual NPs as well as elemental composition on different zones of an individual NP were analysed on a JEOL ARM200F (JEOL Ltd.) cold FEG operating at 120 kV and equipped with TEM / STEM double spherical aberration (Cs) correctors. Scanning transmission electron microscopy - high angle annular dark field

(STEM-HAADF) images were acquired in the angular range of 50-180 mrad with an 8 cm camera length and a 0.1 nm probe size. Elemental compositions and maps were performed by STEM-EDS using a JEOL EDS (Energy Dispersive Spectroscopy) system and a 0.13 nm probe size. Samples were prepared by dispersing a small amount of the materials in ethanol using ultrasound bath. A drop of the solution was deposited onto a holey carbon-coated copper grid.

The crystalline structure of the prepared particles was assessed by X-ray powder diffraction (XRD) using a Panalitycal X'pert Pro diffractometer (CuKα) with an X-Celerator detector over an angular range of $10º < 2\theta < 120º$, 2θ step width of 0.02º, and 10 s counting time. Silicon was used as internal standard. The crystallite size was calculated from the width at half maximum of the (111) reflection using the Scherrer equation and taking into account the instrumental broadening contribution of our equipment. On the other hand, the $Ba_xCe_{1-x}F_{3-x}$ unit cell volume was calculated using the Rietveld method implemented in the TOPAS software (TOPAS version 4.2, Bruker AXS, 2009). Refined parameters were background coefficients, scale factor, zero, unit cell parameters, displacement parameters of Ba^{2+} and Ce^{3+} and profile parameters. The presence of Tb^{3+} in the $Ba_xCe_{1-x}F_{3-x}$ crystal structure was confirmed by determination and comparison of unit cell parameters of the undoped and Tb^{3+}-doped NPs.

The quantitative composition of the different samples was analysed by inductively coupled plasma atomic emission spectroscopy (ICP-AES, Horiba Jobin Yvon, Ultima 2). The powders samples were previously dissolved in hydrochloric acid.

The excitation and emission spectra of the Tb^{3+}-doped NPs dispersed in water (0.5 mg mL^{-1}) were measured in a Horiba Jobin Yvon spectrofluorimeter (Flourolog3). Lifetime measurements were obtained by recording the luminescence decay curve associated to the $^5D_4 \rightarrow {}^7F_5$ transition of Tb^{3+} ions (540 nm) at an excitation wavelength of 262 nm.

For the evaluation of the CT contrast efficiency, aqueous suspensions containing different concentrations of the Ba-Ce NPs were prepared in 1.5 mL Eppendorf tubes. Iohexol solutions with the same concentration as those of NPs in mg/mL were prepared for comparative purposes. The dispersions were placed in a vortex device for 2 min prior to analyses. Each sample (200 μL aliquot) was placed in a multiwell microplate, along with a Milli-Q water sample for calibration. CT images were acquired with a NanoSPECT/CT® (Bioscan), located at the Centro Nacional de Aceleradores (CNA,

Sevilla, Spain). Acquisition parameters included a 106 mA current for a voltage of 75 kV, exposure time per projection of 1500 ms and 360 projections per rotation. The image length was 6 cm, with a pitch of 1. The total acquisition time required was 18 min. The image was reconstructed with Vivoquant image processing software (Invicro), with the exact cone beam filtered back projection algorithm and the Shepp Logan 98 % filter. The resulting image pixel size was uniform in three dimensions at 0.2mm. Images were analysed with PMOD 3.8 software (PMOD Technologies LLC). Spherical volumes of interest (VOIs) of 2 mm radius were made within each sample to calculate the X-ray attenuation (Hounsfield units - HU) for each concentration. Average values of Milli-Q water and dispersions were used to calculate HU values in the images, with attenuation being 0 HU for water and –1000 HU for air.

RESULTS AND DISCUSSION

1. Synthesis, morphology and crystal structure of the $Ba_xCe_{1-x}F_{3-x}$ nanoparticles.

The well-known La Mer and Dinegar model[25] establishes that separation of nucleation and growth processes are necessary to obtain monodisperse particles by homogeneous precipitation. Such precipitation can be achieved through a slow and controlled release of the precipitating anions or cations in the reaction medium[26] to keep a constant precipitation kinetics in the whole solution. A homogeneous precipitation in polyol medium has been used here to obtain uniform Ba-Ce fluoride NPs. Polyols have been used as reaction media because they may act not only as solvents but also as capping agents, thus limiting particle growth.[27] The reaction kinetics has been controlled by using sodium tetrafluoroborate as the fluoride source, which was previously shown to produce a controlled release of fluoride anions to the reaction medium.[28] Following this strategy, we first addressed the synthesis of undoped NPs for simplicity. We found that aging at 120 ºC for 20 hours an EG/H_2O (90/10 V/V) solution containing $NaBF_4$ (0.0875 M), $Ce(NO_3)_3$ (0.05 M) and $Ba(NO_3)_2$ (0.05 M) led to precipitation of homogeneous, spherical NPs with a mean diameter of 80 nm, as shown in the SEM micrograph of **Figure 1a**. The particles surface shows corrugations and roughness that suggest that the spheres are formed through an ordered aggregation of smaller subunits (primary particles), as later confirmed in this work. A progressive decrease of particles diameter was detected when the starting $NaBF_4$ concentration was increased (**Figures 1b-d)**. The mean sphere

diameters, measured from SEM micrographs, have been plotted versus $NaBF_4$ concentration in **Figure 2a (red circles)**, where a clearly linear dependence can be observed. The smallest NPs (50 nm diameter) were obtained using [$NaBF_4$] = 0.30 M. The explanation of such behaviour is a complex task since the final size of particles formed from aggregation of primary units is the result of several processes such as the nucleation and growth of primary units and their further attachment, each of which being affected by several experimental parameters including the reagents concentration. For example, according with the classical model proposed by La Mer and Dinegar,[25] the increase of the $NaBF_4$ concentration is expected to give rise to a faster nucleation rate and consequently, to an increase of the number of nuclei leading to a decrease in the size of the primary units, which might result in smaller final particles. On the other hand, reagents concentration also determines the ionic strength of the reaction medium and therefore, the magnitude of the repulsive forces acting in colloidal systems,[29] which also govern the aggregation extent.

The appropriate experimental conditions to obtain uniform NPs were quite restricted, since the change of any of the experimental parameter required to obtain the NPs shown in Figure 1 − including precursors concentrations, fluoride precursor nature, EG/H_2O ratio, and polyol type− led to non-uniform particles or even heterogeneous or amorphous precipitates (**Figure S1**). These changes must be assigned to variation in the kinetics of precipitation, which also affect the nucleation and growth processes.

Information on the colloidal stability of the synthesised NPs can be obtained from DLS and Zeta potential measurements. DLS curves recorded for aqueous suspensions (pH= 5.4) of the four types of NPs are shown in **Figure 2b**. As observed, the average hydrodynamic diameters are very close to the values obtained from the SEM micrographs for all the NPs, except for the smallest ones (50 nm diameter) whose hydrodynamic diameter was close to 300 nm. This finding clearly reveals a high colloidal stability for the former particles, and the presence of a certain degree of aggregation in the latter case. Such behaviour can be explained by the Zeta potential values measured for such suspensions, which decreased linearly with particle size from +38 mV for the 80 nm NPs down to +20 mV for the 50 nm NPs **(Figure 2a, blue stars)**. It is well known that Zeta potential values ≥ +30mV (or ≤ −30mV for negative Z values) as those obtained for the suspensions of NPs with diameter ≥ 65 nm, are considered to provide enough repulsion forces to avoid particle aggregation. On the contrary, for lower Zeta potential values, the

attractive van der Waals forces become stronger than the repulsive electrostatic forces leading to the aggregation of the NPs, as it is the case of the smaller (50 nm) NPs. The water-dispersible character shown by the as prepared particles indicate their compatibility with physiological fluids, without the need to further treating the samples, as is the case of other Ba-Ce fluoride NPs reported in the literature.[23,30]

The smallest synthesized NPs showing uniform shape, size (65 nm diameter) and colloidal stability were selected for the rest of the experiments reported in this work. These experiments consisted of the study of their crystal structure, chemical nature, optical properties (after doping with Tb^{3+} ions) and X-ray attenuation properties.

The crystal structure of the NPs was analysed by X-ray powder diffraction (XRD). **Figure 3a** shows the experimental XRD pattern, which matches with the pattern corresponding to hexagonal CeF_3 (PDF 04-008-8281, ICDD 2016). No other reflections were observed, indicating the absence of any other crystalline phase. The experimental reflections appeared, however, slightly shifted towards lower 2θ values, suggesting an increase in lattice parameters compared to standard CeF_3. In fact, the unit cell volume, calculated from Rietveld refinement, was 326.48(0.14) $Å^3$, to be compared to 320.86 $Å^3$ as reported in the hexagonal CeF_3 PDF card mentioned above or 320.95 $Å^3$ as described in ICSD card 42470. Given the higher ionic radius of Ba^{2+} (1.42 Å, in VIII coordination) compared with Ce^{3+} (1.14 Å in the same coordination), the observed unit cell volume increase suggests the incorporation of Ba^{2+} into the Ce^{3+} crystallographic sites of the hexagonal CeF_3 unit cell.

The crystallite size, calculated from the width of the (111) reflection (27.7 º2θ) using the Scherrer equation was 14 nm. This value, smaller than the NP diameter, suggests a polycrystalline character of each NP, i.e. that their microstructure could consist of the aggregation of smaller subunits. In effect, the high-resolution TEM micrograph (**Figure 4a**) of a single NP clearly shows an assemblage of nanocrystallites with slight orientation mismatches, i.e. rotations or distortions from one to another, as revealed by the elongated spots observed in the FFT pattern (**Figure 4b**). Such orientation mismatches can also be observed inside a single nanocrystallite (**Figure S2**). At higher magnification (**Figure 4c**), the NP shows very well defined and regularly spaced fringes at 3.2 Å, corresponding to the (111) planes of the hexagonal unit cell, indicating a high crystallinity of the

individual subunits. This result is also obvious from the well-defined spots observed in the FFT pattern (**Figure 4d**) obtained from the green square area presented in Figure 4c.

The EDX spectrum of the NPs performed on the SEM (**Figure 3b**) showed exclusively bands corresponding to barium, cerium and fluoride. The quantitative composition of the NPs was analysed by ICP spectroscopy and revealed a Ba/Ce molar ratio = 0.18/0.82, from which the following chemical formula can be derived: $Ba_{0.18}Ce_{0.82}F_{2.82}$. The observed hexagonal phase for this composition is not in agreement with the BaF_2-CeF_3 phase diagram, which shows a stability field for the hexagonal phase for $x < 0.12$ ($Ba_xCe_{1-x}F_{3-x}$).[31] It is important to note, however, that the present conditions are far away from the thermodynamic equilibria of the reported phase diagram, in which the studied temperature interval was from 870 ºC up to the melting point.

The experimental Ba/Ce ratio (0.18/0.82) in the synthesized NPs strongly contrasts with the nominal value (0.5/0.5). Therefore, many of the Ba^{2+} ions that were added to the starting EG/H_2O solution did not incorporate to the NPs under the experimental synthesis conditions. To check if the mismatch between our nominal and experimental Ba/Ce ratio could be due to different precipitation rates of Ba^{2+} and Ce^{3+} ions, several experiments were carried out in the same conditions as for the synthesis of $Ba_{0.18}Ce_{0.82}F_{2.82}$ NPs (EG/H_2O 90/10, 0.18 M $NaBF_4$, 0.05 M $Ce(NO_3)_3$ and 0.05 M $Ba(NO_3)_2$, 120ºC, 20 hours) but using longer (48 h) and shorter (1h and 4 h) aging times. The corresponding TEM micrographs (**Figure S3, top**) showed that uniform NPs, with the same shape as those obtained after 20 hours aging time were already observed after 1 hour and kept the same morphology for the various reaction durations, with some particle aggregation occurring after 48 hours. However, the Ba/Ce ratio was not constant with aging time (**red circles in Figure 5**), but a pronounced increase was observed from Ba/Ce = 0.08/0.92 to Ba/Ce = 0.18/0.82 when aging time increased from 1 hour to 20 hours, while no appreciable changes were detected for aging times longer than 20 hours. All XRD patterns of the samples aged during different times (**Figure S3, bottom**) showed the same set of reflections, compatible with hexagonal CeF_3, and no reflections coming from other phases were observed in any pattern. The unit cell volume values (**blue stars in Figure 5**) evolved in the same exponential way as the Ba/Ce ratio. These results suggest that, under these experimental conditions, *i)* Ba^{2+} incorporation into the NPs is slower than that of Ce^{3+}, *ii)* there is a superior limit in the amount of Ba^{2+} incorporated into the NPs, *iii)* Ba^{2+} substitutes Ce^{3+} in the hexagonal structure at any of the observed Ba/Ce ratio.

To check whether the limited amount of precipitated Ba^{2+} ions is due to thermodynamic factors, precipitation reactions were carried out using the same experimental conditions as for the $Ba_{0.18}Ce_{0.82}F_{2.82}$ NPs except for the temperature that was progressively increased up to 240 ºC. The Ba/Ce ratio showed an exponential increase with temperature, showing a 0.48/0.52 value at 240 ºC, very close to the nominal one (0.5/0.5) (**Figure 6a**). At this aging temperature, the particles turned less uniform and aggregated themselves (**Figure S4**), so that they were not appropriate for bio-applications. We can conclude, in view of these data, that it is necessary to increase the temperature above 240ºC, to incorporate into the NPs the whole amount of barium initially present in the reaction medium. Finally, to check the influence of the Ba/Ce ratio on the crystalline nature of the precipitated phase at the temperatures of this study, we have recorded the corresponding XRD patterns (**Figure 6b**). While a unique phase (hexagonal CeF_3-type phase) was observed at 120ºC, reflections corresponding to cubic BaF_2 (PDF 00-004-0452, ICDD 2016) emerged from the pattern of the sample aged at 150 ºC (corresponding to a Ba/Ce ratio of 0.37/0.63), although the reflections were clearly shifted to higher 2θ value, suggesting the presence of Ce^{3+} in the BaF_2 structure. The intensity of such reflections increased with increasing aging temperature while those corresponding to the hexagonal phase decreased. The percentage of each phase calculated from Rietveld refinement is shown in **Figure 6c**. Coexistence of both phases could still be observed at the highest temperature of this study (240 ºC, corresponding to Ba/Ce = 0.48/0.52). Observation of both phases at Ba/Ce ratios between 0.37/0.63 and 0.48/0.52 is in good agreement with the BaF_2-CeF_3 phase diagram, which indicates that the hexagonal and cubic phases coexist in the interval $0.12 < x < 0.48$ while the cubic phase is the only stable phase at higher x values.[31]

2. Synthesis and characterization of Tb^{3+}:$Ba_{0.18}Ce_{0.82}F_{2.8}$ nanoparticles.

Ba-Ce fluoride NPs doped with different Tb^{3+} contents (nominal Tb/Ce = 2.5 %, 5 %, 10 %, and 15 %) were synthesized using the method reported above for the undoped 65 nm $Ba_{0.18}Ce_{0.82}F_{2.8}$ NPs, and adding the corresponding amount of terbium nitrate in each case. It was found that the doping process did not alter the shape nor the size of the particles up to 10 % doping level, while higher Tb^{3+} contents led to aggregated particles (**Figure S5**).

The XRD patterns of the doped samples were very similar to the undoped material and no extra reflexions were observed at any doping level (**Figure 7a**). The unit cell volume

values decreased linearly with increasing Tb^{3+} content (**Figure 7b**), which indicates that Tb^{3+} is located in the unique Ba/Ce crystallographic site of the hexagonal structure.

In order to analyse the cations distribution throughout one individual nanoparticle, two different analytical approaches were applied using the 10% Tb doped sample as an example. First, we have recorded the STEM-EDS Ba, Ce, Tb mapping on the nanoparticle shown in **Figure 8a** and plotted in **Figure 8b**. A homogeneous distribution of Ba, Ce and Tb can be observed all through the nanoparticle, with no signs of chemical segregation. Likewise, punctual STEM-EDS analyses recorded on different regions of the NP (marked with blue squares in Figure 8a) showed very similar values for each element, as shown in **Figure 8c**, which confirms the homogeneous distribution of cations in the NP. The mean Tb/Ce ratio obtained from these analyses was 12.8(s.d. 2.5) %, which was close to the 10 % nominal value.

3. Luminescence of the Tb^{3+}:$Ba_{0.18}Ce_{0.82}F_{2.8}$ nanoparticles.

It is well known that the green luminescence of Tb^{3+} is usually weak as the electronic transitions within the $4f^n$ configuration of Tb^{3+} are strongly forbidden. In the presence of Ce^{3+}, however, the intensity of the emission is greatly increased through an energy transfer (ET) process from Ce^{3+} to Tb^{3+} ions.[32] Such ET is possible because the emission band of Ce^{3+} matches well with the *f* - *f* absorptions of Tb^{3+} ions. In fact, the excitation spectrum of the undoped sample monitored at the characteristic Ce^{3+} emission wavelength (345 nm) showed an intense band centred at 259 nm, corresponding to the optically allowed transitions from *4f* to *5d* states of Ce^{3+} (**Figure 9a,** blue curve). This band is also present in the spectrum of the 10% Tb^{3+} doped sample monitored at the characteristic Tb^{3+} emission wavelength (540 nm) (**Figure 9a,** green curve), which proves the mentioned ET process. The latter spectrum shows, in addition, a set of much weaker excitation bands (with maxima at 351 nm and 378 nm) corresponding to the transitions from Tb^{3+} $^7F_6$ ground state into the higher excited states. These transitions are parity-forbidden, which explains their low intensity.

The emission spectrum of the undoped sample under an excitation wavelength of 262 nm (blue curve in **Figure 9b**) showed a unique broad band, between 300 nm and 400 nm, which is due to the electronic transition from *5d* to *4f* state of Ce^{3+}.[32] The excitation energy of Tb^{3+} ions is inside this range, and this fact explains the ET from Ce^{3+} to Tb^{3+}. The excitation spectra of the Tb-doped samples, under the same excitation wavelength

(**Figure 9b**) contain, in addition to the Ce^{3+} band, a set of sharp emission peaks that originate from the *4f-4f* transitions of Tb^{3+} labelled in the figure. It can be observed that increasing the Tb^{3+} doping level induces an increase in the emission intensity of the Tb^{3+} bands while the emission band of Ce^{3+} decreases, which again evidences the Ce^{3+}-Tb^{3+} energy transfer process. The Ce^{3+}-Tb^{3+} ET efficiency (η_{ET}) has been calculated for each doped sample according to the formula

$$\eta_{ET} = I_{Tb}/(I_{Tb} + I_{Ce}) \qquad (1)$$

where I_{Tb} and I_{Ce} are the integral areas of the Ce^{3+} and Tb^{3+} emission bands, respectively. Efficiency values of 32%, 38% and 65% were obtained for the 2.5 %, 5 %, and 10 % nominal Tb^{3+}-doped samples, respectively. The increase of ET efficiency with increasing Tb^{3+} doping level is in good agreement with the Ce^{3+}-Tb^{3+} ET process.

The luminescence dynamics of the Tb-doped NPs was analysed from the fluorescence decay curve of the $^5D_4 \rightarrow {}^7F_4$ transition (540 nm) in the sample that showed the maximum emission intensity (10% Tb^{3+}-doped NPs). The curve, shown in **Figure 9c**, showed an exponential decay that could be fitted using a biexponential temporal dependence of the form:

$$I(t) = I_1 \exp(-t/\tau_1) + I_2 \exp(-t/\tau_2) \qquad (2)$$

where *I(t)* is the luminescence intensity, *t* is the time after excitation, and τ_i (i = 1, 2) is the decay time of the *i* component, with intensity I_i. The parameters obtained from the fitting were τ_1 = 6.88 ms (I_1= 68%) and τ_2= 1.61 ms (I_2 = 32%). The long lifetime has classically been assigned to the luminescent centers located in the interior of the nanoparticle while the short lifetime values correspond to the surface ions, where the presence of impurities such as hydroxyl species, act as luminescence quenchers, thus increasing the decay rate.[33]

The average decay time, $\langle\tau\rangle$, obtained from the following equation,

$$\langle\tau\rangle = \frac{\int_{t_0}^{t_f} tI(t)dt}{\int_{t_0}^{t_f} I(t)dt} = \left(\tau_1^2 I_1 + \tau_2^2 I_2\right)/\left(\tau_1 I_1 + \tau_2 I_2\right) \qquad (3)$$

was 6.36 ms. This value was considerably higher than that reported for cubic 10% Tb-doped $BaCeF_5$ nanocrystals (1.66 ms).[34] The difference in lifetime could be assigned to the different, morphology, symmetry and/or Ba/Ce ratio of the particles. However, given that the latter features are related to one another, that is, the symmetry is composition-dependent, it is not possible to discern about the influence of both parameters on the phosphor efficiency.

4. X-ray attenuation properties of 10% Tb-doped $Ba_{0.18}Ce_{0.82}F_{2.8}$ nanoparticles.

X-ray computed tomography contrast agents (also called CT contrast agents) are used in bioimging to enhance the contrast between tissues with similar and/or low X-ray attenuation by increasing the local attenuation without increasing the radiation dose to the patient. Clinically approved X-ray contrast agents include barium sulfate suspensions and iodinated molecules. In the last few years, several lanthanide-based NPs have also been proposed as CT contrast agents due to their high ability to absorb X-rays because of the high atomic number of lanthanides.[35] Based on the high atomic number of the components of our NPs (Z_{Ba}=56, Z_{Ce}=58 and Z_{Tb}=65) we postulate that they might present good X-ray attenuation properties. To validate the CT contrast agent efficiency of the Tb-doped Ba-Ce fluoride NPs we selected the sample that proved optimum luminescence (10% Tb). X-ray CT phantom images were acquired using different mass concentrations of the NPs in deionized water. As shown in **Figure 10a**, the attenuation was gradually increased with increasing concentration of the NPs, while the contrast produced with the same concentrations of Iohexol, a clinically approved iodinated molecule, was much weaker. The X-ray absorption values of both Iohexol and NPs in HU (**Figure 10b**) show a linear increase with suspension concentration with a higher slope in the case of the NPs. A local X-ray attenuation change of about 100 HU is recommended to obtain enough contrast in the CT image. To obtain such value, we need about 10 mg/mL Iohexol and only 5 mg/mL of the NPs, which proves the superior performance of the Ba-Ce fluoride NPs as promising CT contrast agents.

CONCLUSIONS

Uniform $Ba_{0.18}Ce_{0.82}F_{2.8}$ nanospheres with a diameter of 65 nm have been synthesized by a solvothermal method using very restrictive experimental conditions including the use

of $NaBF_4$ as the fluoride source. The obtained nanoparticles are polycrystalline, present hexagonal crystal symmetry and show colloidal stability in water. It was found that, although a nominal Ba/Ce molar ratio of 0.5/0.5 was used in the reaction, the experimental Ba/Ce ratio was temperature dependent, with values ranging from 0.18/0.82 at 120ºC to 0.48/0.52 at 240 ºC. Increasing synthesis temperature resulted in a phase transition from hexagonal to cubic symmetry and in the loss of colloidal stability. The NPs diameter could be modified from 65 nm to 80 nm, using different $NaBF_4$ concentrations, while maintaining the uniformity and colloidal stability of the NPs. The proposed method was also successful to synthesise Tb^{3+}-doped $Ba_{0.18}Ce_{0.82}F_{2.8}$ NPs with the same morphological features as the undoped material as long as the doping level was ≤ 10% Tb. The Tb-doped NPs showed an intense emission under UV excitation thanks to the Ce-Tb energy transfer phenomenon, the 10%-doped sample showing the highest emission intensity. Finally, it was demonstrated that aqueous suspensions of the latter NPs showed significantly higher X-ray attenuation values than suspensions of the same concentration of Iohexol, a clinically approved CT contrast agent. The excellent luminescence and X-ray attenuation properties of the Tb-doped Ba-Ce fluoride nanospheres, together with their hydrophilic character, suggest potential applications as dual bioprobes for luminescence bioimaging and computed tomography.

CONFLICTS OF INTEREST

There are no conflicts to declare.

ACKNOWLEDGEMENTS

Marcin Balzercyk (CNA, Sevilla, Spain) is gratefully acknowledged for help with CT. Dr. Auriane Etienne from GPM Rouen is gratefully acknowledged for the access to the TEM JEOL ARM 200F. This TEM is a part of GENESIS plateform. GENESIS is supported by the Région Haute-Normandie, the Métropole Rouen Normandie, the CNRS via LABEX EMC and the French National Research Agency as a part of the program "Investissements d'avenir" with the reference ANR-11-EQPX-0020. This work was supported by CSIC projects (PIC2016FR1, PIE 201560E056, and PIE201460E005). This work was supported in part by Siemens Healthcare S.L.U.

REFERENCES

1 G. Wang, Q. Peng, Y. Li, *Acc. Chem. Res.* 2011, **44**, 322 – 332.
2 H. Dong, S.R. Du, X.Y. Zheng, G.M. Lyu, L.D. Sun, L.D. Li, P.Z. Zhang, C. Zhang, C.H. Yan, *Chem. Rev.* 2015, **115**, 10725−10815.
3 R. An, P. Lei, P Zhang, X. Xu, J. Feng, H. Zhang, *Nanoscale* 2018, 10, 1394-1402.
4 X. Ding, J. Liu, D. Liu, J. Li, F. Wang, L. Li, Y. Wang, S. Song, H. Zhang, *Nano Res.*, 2017, **10**, 3434–3446.
5 D. Ni, W. Bu, E.B. Ehlerding, W. Cai, J. Shi, *Chem. Soc. Rev.* 2017, **46**, 7438-7468.
6 D. González-Mancebo, A.I. Becerro, T.C. Rojas, M.L. García-Martín, J.M. de la Fuente, M. Ocaña, *Part. Part. Syst. Charact.* 2017, **34**, 1700116.
7 P. Cortelletti, M. Pedroni, F. Boschi, S. Pin, P. Ghigna, P. Canton, F. Vetrone, A. Speghini, *Cryst. Growth Des.* 2018, **18**, 686-694.
8 C. Li, Z. Hou, C. Zhang, P. Yang, G. Li, Z. Xu, Y. Fan, J. Lin, *Chem. Mater.* 2009, **21**, 4598–4607.
9 F. Wang, J. Wang, X. Liu, *Angew. Chem.* 2010, **122**, 7618-7622.
10 N. Hoshyar, S. Gray, H. Han, G. Bao, *Nanomedicine (Lond.)* 2016, **11**, 673–692.
11 Z. Wang, C. Liu, L. Chang, Z. Li, *J. Mater. Chem.* 2012, **22**, 12186–12192.
12 R. Naccache, Q. Yu, J.A. Capobianco, *Adv. Opt. Mater.* 2015, **3**, 482-509.
13 Y. Huang, Q. Xiao, H. Hu, K. Zhang, Y. Feng, F. Li, J. Wang, X. Ding, J. Jiang, Y. Li, L. Shi, H. Lin, *Small* 2016, **12**, 4200–4210.
14 C. Lorbeer, A.V. Mudring, *J. Phys. Chem.* C 2013, **117**, 12229-12238.
15 M. Quintanilla, N.O. Nuñez, E. Cantelar, M. Ocaña, F. Cusso, *Nanoscale* 2011, **3**, 1046-1052.
16 T Samanta., S. Sarkar, V.N.K.B. Adusumalli, A.E. Praveen, V. Mahalingam, *Dalton Trans.* 2016, **45**, 78-84.
17 S. Rodriguez-Liviano, N.O. Nuñez, S. Rivera-Fernandez, J.M. de la Fuente, M. Ocaña, *Langmuir* 2013, **29**, 3411-3418.
18 J. Zhuang, L. Liang, H. H. Y. Sung, X. Yang, M. Wu, I.D. Williams, S. Feng, Q. Su, *Inorg. Chem.* 2007, **46**, 5404−5410.
19 D. Yang, Y. Dai, P. Ma, X. Kang, Z. Cheng, C. Li, J. Lin, *Chem. Eur. J.* 2013, **19**, 2685 – 2694.
20 X. Li, S. Gai, C. Li, D. Wang, N. Niu, F. He, P. Yang, *Inorg. Chem.* 2012, **51**, 3963−3971.
21 H.R. Liu, W. Lu, H.B. Wang, L. Rao, Z.G. Yi, S.J. Zeng, J.H. Hao, *Nanoscale* 2013, **5**, 6023-6029.
22 D. González-Mancebo, A.I. Becerro, E. Cantelar, F. Cussó, A. Briat, D. Boyer, M. Ocaña, *Dalton Trans.* 2017, **46**, 6580-6587.
23 D. Chen, Y. Yu, F. Huang, Y. Wang, *Chem. Commun.* 2011, **47**, 2601–2603.
24 T. Sheng, Z. Fu, X. Wang, S. Zhou, S. Zhang, Z. Dai, *J. Phys. Chem. C* 2012, **116**, 19597−19603.
25 V. K. LaMer, R.H. Dinegar, *J. Am. Chem. Soc.* 1950, **72**, 4847−4854.
26 E. Matijevic, *Chem. Mater.* 1993, **5**, 412.
27 C. Feldmann, *Adv. Funct. Mater.* 2003, **13**, 101.
28 H. Guan, Y. Sheng, Y. Song, C. Xu, X. Zhou, K. Zheng, Z. Shi., H. Zou, *J. Phys. Chem. C* 2017, **121**, 23080-23095.
29 B. Derjaguin, L. Landau, *Acta Physicochim URSS* 1941, **14**, 633–662.
30 L. Lei, D. Chen, F. Huang, Y. Yu, Y. Wang, *J Alloys Comp.* 2012, **540**, 27–31.
31 B.P. Sobolev, N.L. Tkachenko, *J. Less Common Met.* 1982, **85**, 155–170.

32 G. Blasse, A. Brill, *J. Chem. Phys.* 1967, **47**, 1920–1926.
33 J.W. Stouwdam, F.C.J.M. Van Veggel, *Nano Lett.* 2002, **2**, 733-737.
34 T. Sheng, Z. Fu, J. Wang, X. Fu, Y. Yu, S. Zhou, S. Zhang, Z. Dai, *RSC Adv.* 2012, **2**, 4697–4702.
35 M. Laguna, N.O. Núñez, F.J. Garcia, A. Corral, A. Parrado-Gallego, M. Balcerzyk, A.I. Becerro, M. Ocaña, *Eur. J. Inorg. Chem.* 2017, 5158–5168.

Figure captions:

Figure 1: SEM micrographs of NPs obtained after aging at 120ºC for 20 hours an EG/H_2O solution containing $Ba(NO_3)_2$ (0.05 M) and $Ce(NO_3)_3$ (0.05 M) and different concentration of $NaBF_4$: 0.0875 M (a); 0.125 M (b); 0.180 M (c) and 0.300 M (d)

Figure 2: a) Evolution of NPs diameter (obtained from SEM micrographs) and Zeta potential values with the concentration of $NaBF_4$ used in the synthesis. b) DLS plots showing the particle size distribution in aqueous suspensions of NPs synthesized using different $NaBF_4$ concentrations

Figure 3: Experimental XRD pattern (a) and EDX spectrum (b) of the 65 nm diameter NPs. Blue lines in (a) are the reflections of PDF 04-008-8281, corresponding to hexagonal CeF_3

Figure 4: a) HREM micrograph of a $Ba_{0.18}Ce_{0.82}F_{2.82}$ NP; b) FFT pattern obtained from (a) image. c) Magnification of the red square in (a); d) FFT obtained from the green square in (c)

Figure 5: Evolution, with increasing aging time, of Ba/Ce ratio and unit cell volumes corresponding to $Ba_xCe_{1-x}F_{3-x}$ NPs synthesized in the experimental conditions of Figure 1c

Figure 6: a) Evolution, with increasing aging temperature, of the Ba/Ce ratio corresponding to $Ba_xCe_{1-x}F_{3-x}$ NPs synthesized in the experimental conditions of Figure 1c. b) Experimental XRD patterns of the samples shown in (a). The lines at the bottom of plot correspond to the reflections of hexagonal CeF_3 (PDF 01-070-0002) (red line) and cubic BaF_2 (PDF 00-0004-0452) (black line). Dashed lines are guides to the eye to better observe the shift of reflections with respect to cubic BaF_2. c) Weight % of hexagonal and cubic phases versus aging temperature

Figure 7: XRD patterns (a) and unit cell volume (b) of NPs with different Tb^{3+} doping levels

Figure 8: a) STEM-HAADF image of a 10%Tb^{3+}-doped NP. b) Ba, Ce, Tb and merged EDX mappings on the NP shown in (a). c) Ba, Ce and Tb atomic % values obtained from local EDX analyses recorded on the blue squares shown in (a)

Figure 9: a) Excitation photoluminescence spectra of undoped (blue line) and 10% Tb^{3+}-doped NPs monitored at 345 nm and 540 nm, respectively. b) Emission spectra of undoped and Tb^{3+}-doped NPs recorded at 262 nm excitation wavelength. c) Luminescence decay curve (green crosses) obtained from the $^5D_4 \rightarrow {}^7F_4$ transition (540 nm) in the 10% Tb^{3+}-doped sample after excitation at 262 nm. The red line is the fitting curve obtained using a biexponential temporal dependence, as explained in the text

Figure 10: a) In vitro X-ray computed tomography images of suspensions of 10% Tb^{3+}–doped NPs and Iohexol at different concentrations. b) X-ray attenuation values (in HU) of aqueous suspensions of 10% Tb–doped NPs and Iohexol versus their concentration. Error bars are standard deviations of the attenuation value within VOI

Figure 1

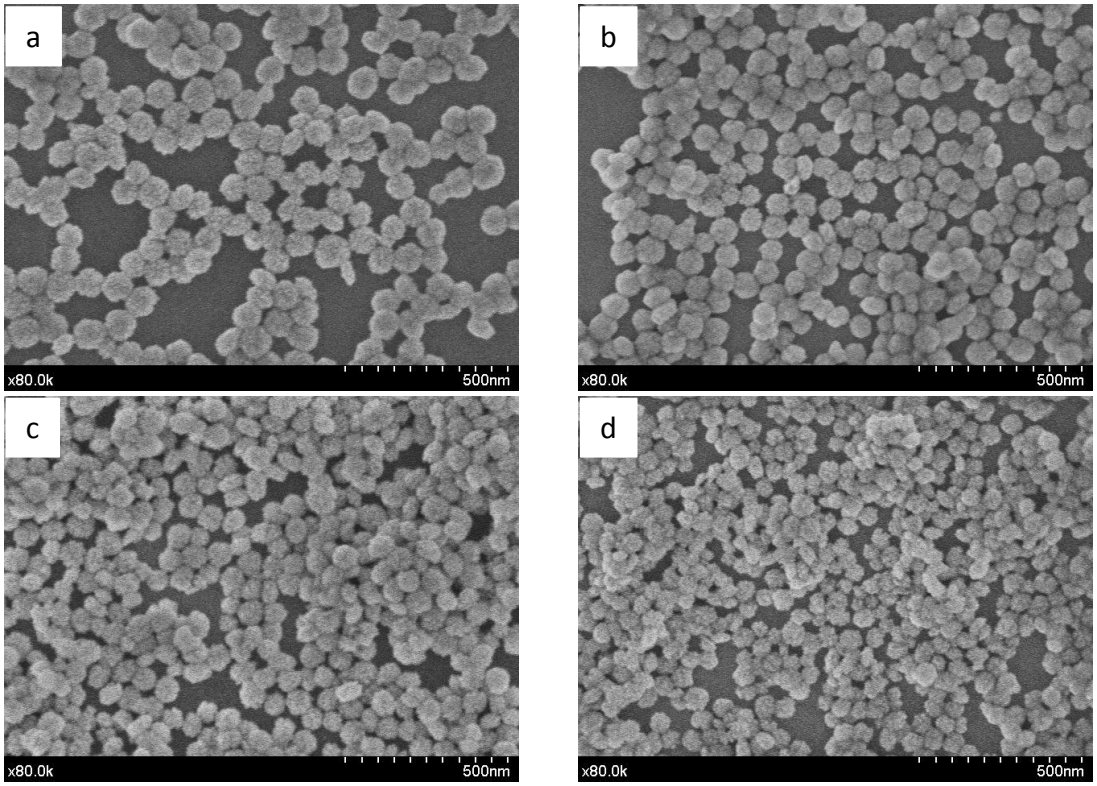

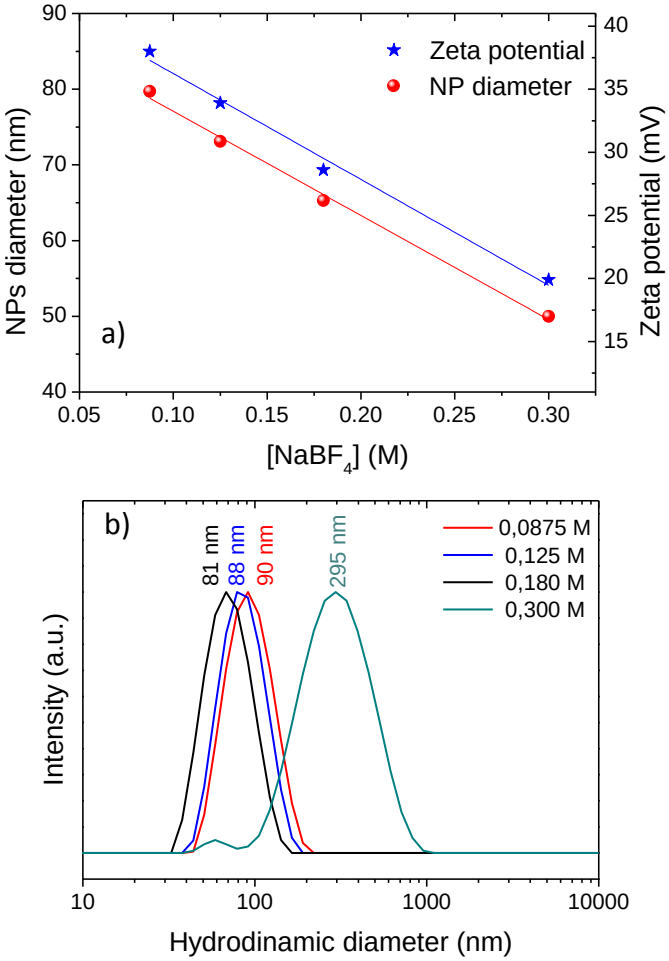
a)
Zeta potential
NP diameter
NPs diameter (nm)
Zeta potential (mV)
[NaBF4] (M)
b)
81 nm
88 nm
90 nm
295 nm
0,0875 M
0,125 M
0,180 M
0,300 M
Intensity (a.u.)
Hydrodinamic diameter (nm)

Figure 3

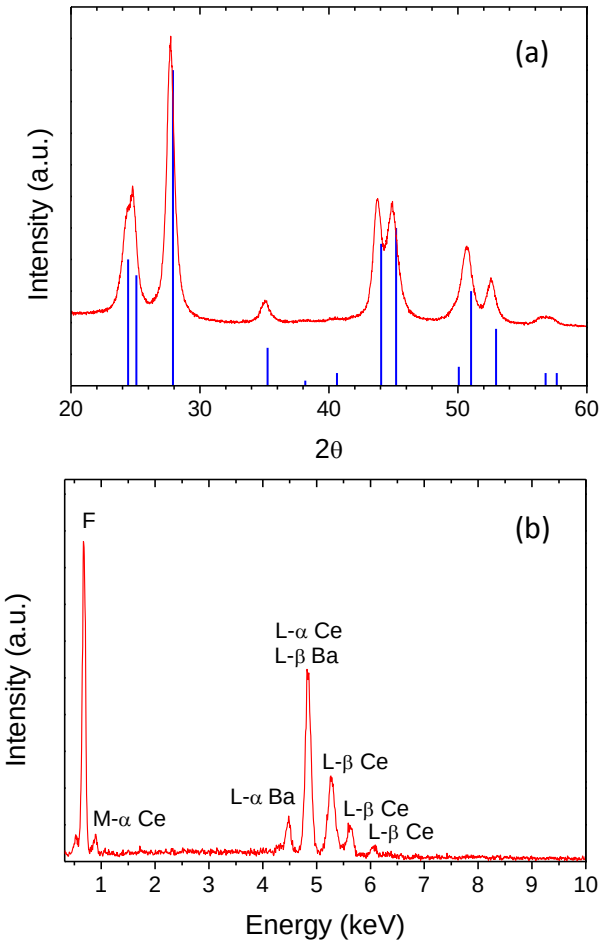
(a)
Intensity (a.u.)
20
30
40
50
60
2θ
(b)
F
L-α Ce
L-β Ba
L-β Ce
L-α Ba
M-α Ce
L-β Ce
L-β Ce
Intensity (a.u.)
1
2
3
4
5
6
7
8
9
10
Energy (keV)

Figure 4

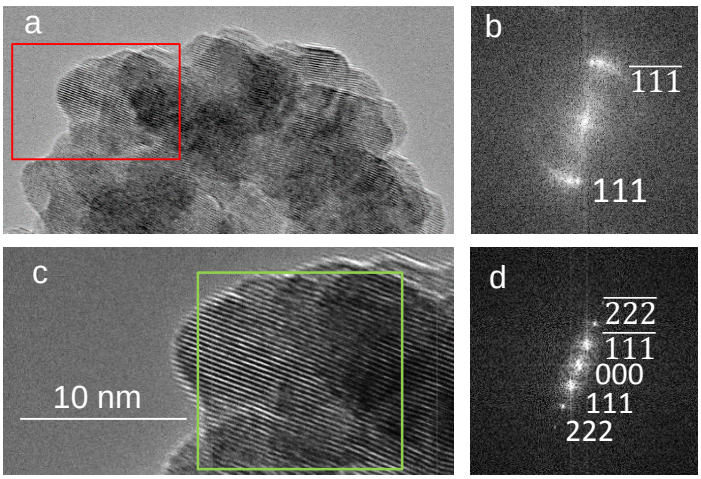
a
b
$\overline{111}$
111
c
10 nm
d
$\overline{222}$
$\overline{111}$
000
111
222

Figure 5

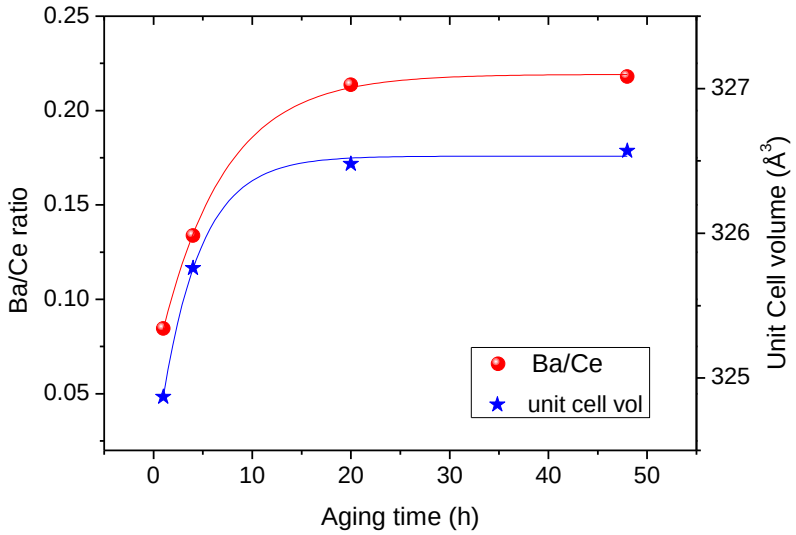
0.25
0.20
0.15
0.10
0.05
Ba/Ce ratio
0
10
20
30
40
50
Aging time (h)
327
326
325
Unit Cell volume (Å3)
Ba/Ce
unit cell vol

Figure 6

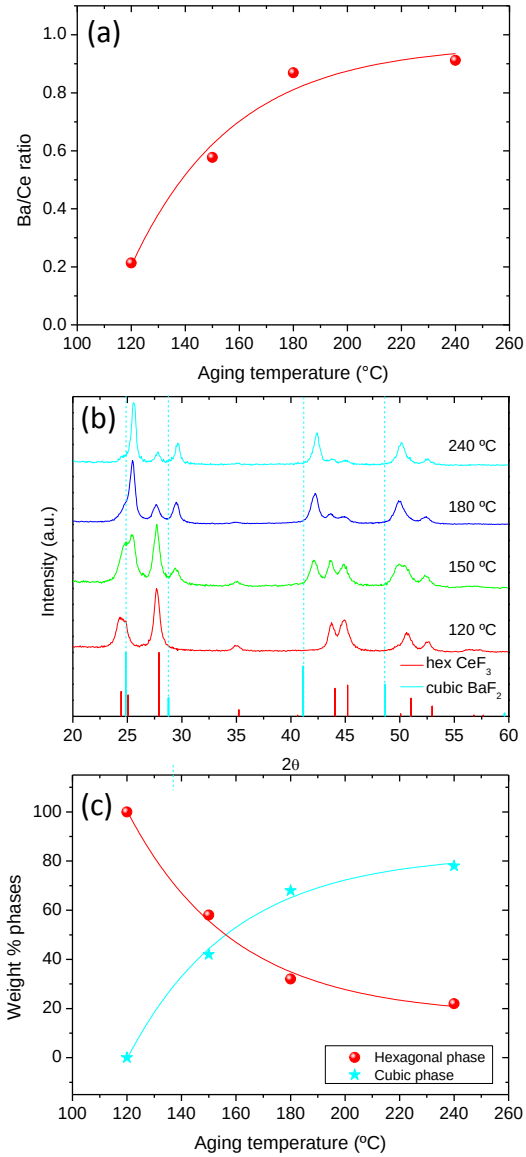
(a)
Ba/Ce ratio
Aging temperature (°C)
(b)
240 ºC
180 ºC
150 ºC
120 ºC
hex CeF3
cubic BaF2
Intensity (a.u.)
2θ
(c)
Weight % phases
Hexagonal phase
Cubic phase
Aging temperature (ºC)

Figure 7

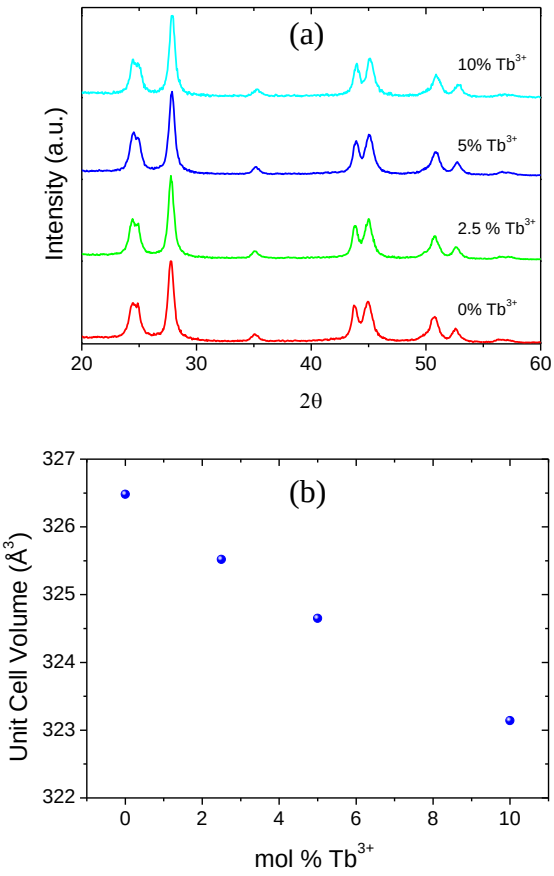
(a)
10% Tb3+
5% Tb3+
2.5 % Tb3+
0% Tb3+
Intensity (a.u.)
20
30
40
50
60
2θ
(b)
Unit Cell Volume (Å3)
327
326
325
324
323
322
0
2
4
6
8
10
mol % Tb3+

Figure 8

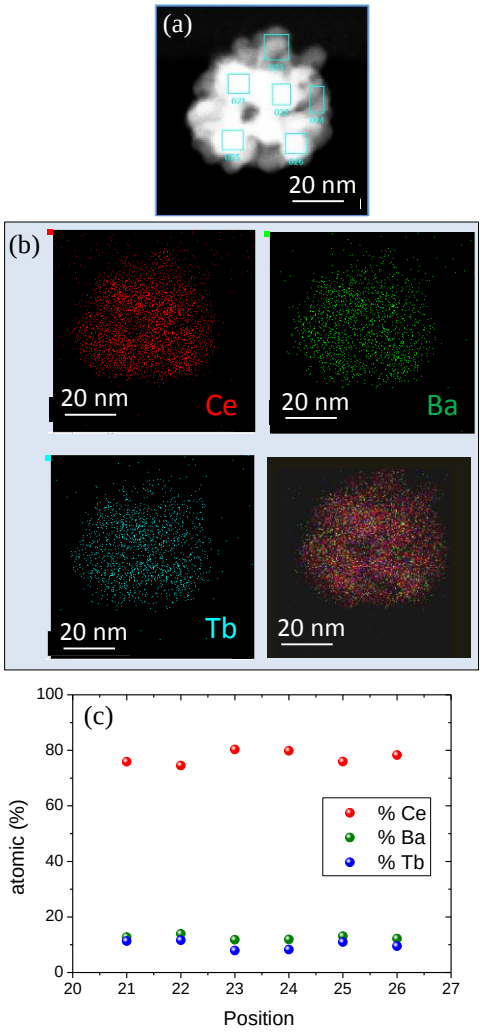
(a)
20 nm
(b)
20 nm
Ce
20 nm
Ba
20 nm
Tb
20 nm
(c)
atomic (%)
Position
% Ce
% Ba
% Tb
0
20
40
60
80
100
20
21
22
23
24
25
26
27

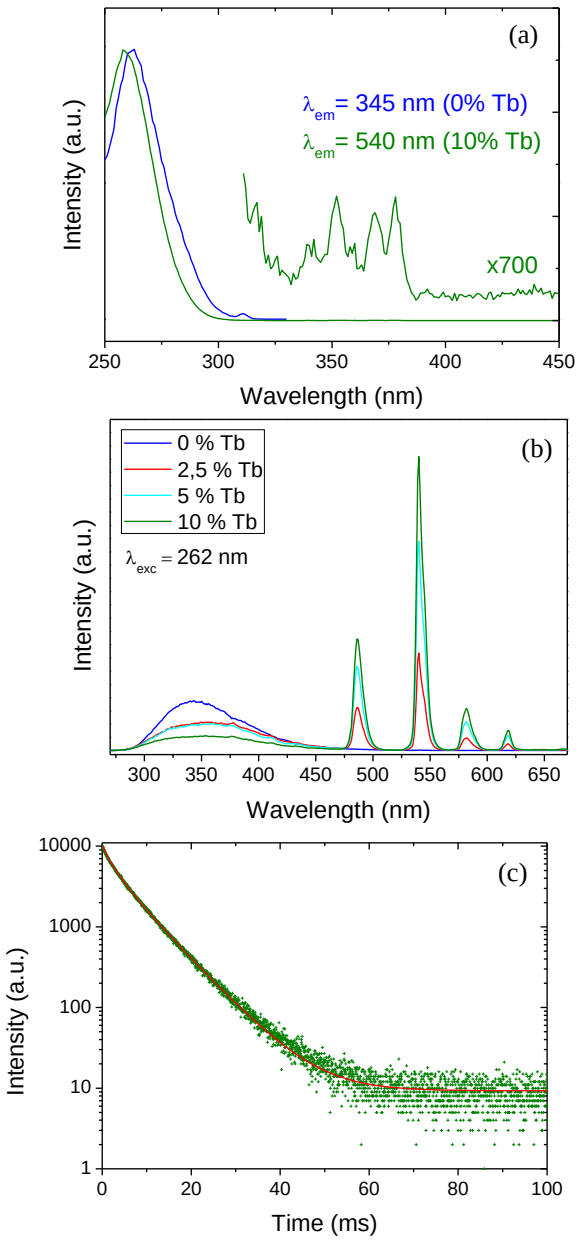
(a)
λem= 345 nm (0% Tb)
λem= 540 nm (10% Tb)
x700
Intensity (a.u.)
250
300
350
400
450
Wavelength (nm)
(b)
0 % Tb
2,5 % Tb
5 % Tb
10 % Tb
λexc = 262 nm
Intensity (a.u.)
300
350
400
450
500
550
600
650
Wavelength (nm)
(c)
10000
1000
100
10
1
Intensity (a.u.)
0
20
40
60
80
100
Time (ms)

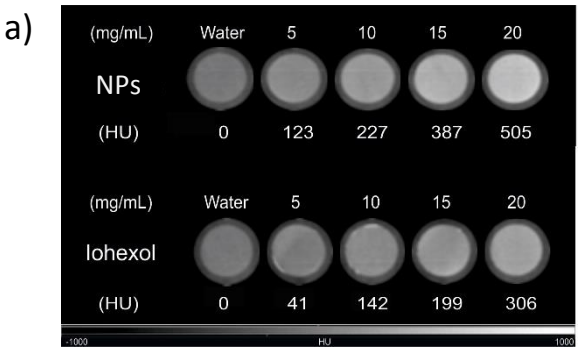
a)
(mg/mL)
Water
5
10
15
20
NPs
(HU)
0
123
227
387
505
(mg/mL)
Water
5
10
15
20
Iohexol
(HU)
0
41
142
199
306
-1000
HU
1000

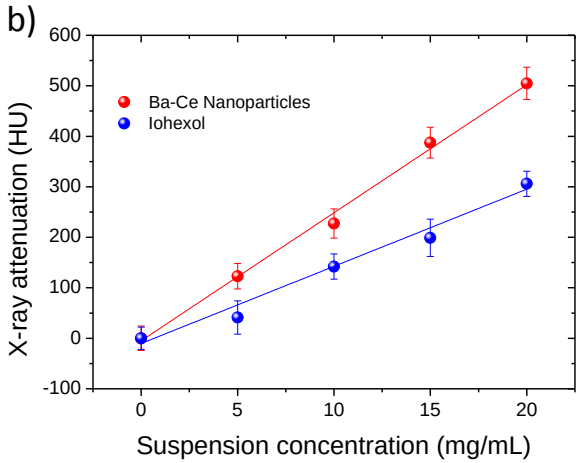
b)
600
500
400
300
200
100
0
-100
X-ray attenuation (HU)
Ba-Ce Nanoparticles
Iohexol
0
5
10
15
20
Suspension concentration (mg/mL)

SYNOPSIS: Uniform Tb^{3+}:$Ba_xCe_{1-x}F_{3-x}$ nanospheres obtained in polyol medium form colloidal suspensions in water and show an intense green emission under UV excitation and excellent X-ray attenuation properties.

TABLE OF CONTENTS GRAPHIC: